

Region-oriented CT image representation for reducing computing time of Monte Carlo simulations

David Sarrut^{a)}

Leon Berard Cancer Center, 28 rue Laennec, 69373 Lyon cedex 08, France and CREATIS Laboratory (UMR CNRS 5220, Inserm U 630), INSA, Bat. Blaise Pascal, av. Jean Capelle, 69621 Villeurbanne cedex, France

Laurent Guigues

CREATIS Laboratory (UMR CNRS 5220, Inserm U 630), INSA, Bat. Blaise Pascal, av. Jean Capelle, 69621 Villeurbanne cedex, France

(Received 1 June 2007; revised 29 November 2007; accepted for publication 3 January 2008; published 17 March 2008)

Purpose. We propose a new method for efficient particle transportation in voxelized geometry for Monte Carlo simulations. We describe its use for calculating dose distribution in CT images for radiation therapy. **Material and methods.** The proposed approach, based on an implicit volume representation named segmented volume, coupled with an adapted segmentation procedure and a distance map, allows us to minimize the number of boundary crossings, which slows down simulation. The method was implemented with the GEANT4 toolkit and compared to four other methods: One box per voxel, parameterized volumes, octree-based volumes, and nested parameterized volumes. For each representation, we compared dose distribution, time, and memory consumption. **Results.** The proposed method allows us to decrease computational time by up to a factor of 15, while keeping memory consumption low, and without any modification of the transportation engine. Speeding up is related to the geometry complexity and the number of different materials used. We obtained an optimal number of steps with removal of all unnecessary steps between adjacent voxels sharing a similar material. However, the cost of each step is increased. When the number of steps cannot be decreased enough, due for example, to the large number of material boundaries, such a method is not considered suitable. **Conclusion.** This feasibility study shows that optimizing the representation of an image in memory potentially increases computing efficiency. We used the GEANT4 toolkit, but we could potentially use other Monte Carlo simulation codes. The method introduces a tradeoff between speed and geometry accuracy, allowing computational time gain. However, simulations with GEANT4 remain slow and further work is needed to speed up the procedure while preserving the desired accuracy. © 2008 American Association of Physicists in Medicine. [DOI: [10.1118/1.2884854](https://doi.org/10.1118/1.2884854)]

Key words: Monte Carlo simulation, particles navigation, voxels

I. INTRODUCTION

In radiation therapy, simulations are used to compute the three-dimensional (3D) dose distribution within a patient's body from a given set of irradiation parameters. Monte Carlo (MC) methods allow accurate simulation of the physical interactions of irradiation particles within patient tissues with photon/electron beams used in conventional radiotherapy,¹ but also with proton² or carbon³ beams used in hadrontherapy. Amongst other applications, MC simulations are a promising basis for designing fast treatment planning systems based on analytical simulations.

The present article will focus on a condensed simulation model that simulates the global effects of collisions in the course of a given step, but uses approximations. Condensed MC is known to track particles on a step-by-step basis.⁴ There are two types of steps: Physical steps transport particles and simulate physical processes (e.g., photoelectric effect, Compton scattering, etc.) in homogeneous media,

whereas geometrical steps take into account the spatial environment of the particle and occur when it passes from a medium to another during transport.

Generally, the anatomical representation of the patient's organs is obtained from a computerized tomography (CT) image. Such a spatial description requires a large amount of data. In Ref. 5, the authors have used about 38 million voxels. Besides the need for computer memory, the lengthy processing time limits the use of MC. Besides using more powerful computers, several other approaches are currently under study to reduce the computational time. For example, several authors have used variance reduction,⁶ optimized energy or production cuts.⁷⁻⁹ Hybrid approaches combining analytical models and MC simulation have also been proposed.¹⁰ All these methods either decrease the number of physical steps or accelerate the stepping process.

At least two possibilities exist to reduce the computational burden due to complex geometry: Either reduce the complexity of the scene or speed up the geometrical stepping

algorithm. We propose a new approach here to fasten the simulation when representing a 3D image using a MC code. It is based on allowing particles to cross voxel boundaries between two similar materials. The principle is not new since several authors have proposed comparable approaches, for example, for DOSXYZnrc (EGSnrc) code.^{11,12} However, the way such boundaries are removed is different since in our case, the transportation algorithm is not modified and thus any algorithm can be used. Instead, a new volume representation was defined, and we used a distance map to efficiently return to the transportation engine the distance to the nearest real boundary. Moreover, the method was implemented in the GEANT4 toolkit. To our knowledge, similar approaches have not been published before. This method can be coupled with other acceleration techniques (e.g., variance reduction, use of parallel machines, etc.) to further decrease simulation times.

This article is organized as follows. Section II describes the state-of-the-art procedure to prepare a CT image in order to use it in a MC simulation (Sec. II A) and the existing representations allowing to handle it in GEANT4 (Sec. II B). Section III describes the proposed approach, which consists of an optimized image representation (Sec. III A) for CT data, which have been preprocessed by an adequate image segmentation procedure (Sec. III B). Section IV describes and discusses three series of experiments that we have carried out in order to evaluate the newly proposed method in comparison to existing ones. Section V finally concludes.

II. EXISTING IMAGE REPRESENTATIONS FOR PARTICLE TRACKING

II.A. From CT image to tissue composition

In order to represent a patient's anatomy given by a CT image in a MC simulation, it is necessary to associate each voxel of the image with a given tissue composition. A material m is defined by a mass density ρ (g cm^{-3}) and an element weight vector denoted by $\omega_i \in [0; 1]$, with $\sum_i \omega_i = 1$. The MC simulator uses such a description to load cross-sectional data files and compute physics tables. The image acquisition process of a CT is the measure of the attenuation coefficients (μ , expressed in Hounsfield units, H) of traversed tissues. H are obtained with Eq. (1) (Ref. 13), where $\mu(E)$ is the linear attenuation coefficient of a tissue $m = (\rho, \{\omega_i\})$ at energy E [see Eq. (2)], with N_A (mol^{-1}) the Avogadro constant, i the element index, and σ_i the total cross section of the physical processes involved during the image acquisition,

$$H = \left(\frac{\mu}{\mu_{\text{water}}} - 1 \right) \times 1000, \quad \mu = \frac{H - H_{\text{air}}}{H_{\text{water}} - H_{\text{air}}}, \quad (1)$$

$$\mu(E) = \rho N_A \sum_{i=1}^n \left(\frac{\omega_i}{A_i} \sigma_i(E) \right). \quad (2)$$

A stoichiometric calibration method to establish a relationship between H and tissue compositions has been proposed by Schneider *et al.*¹⁴ Images of phantoms made up of materials with known compositions and densities are used to

calibrate the CT scanner. The authors have assigned the known materials to the measured H . Materials corresponding to intermediate H values have been interpolated, both in terms of atomic composition and density according to Eqs. (3) and (4)

$$\rho = \frac{\rho_1 H_2 - \rho_2 H_1 + (\rho_2 - \rho_1) H}{H_2 - H_1}, \quad (3)$$

$$\omega_i = \frac{\rho_1 (H_2 - H)}{(\rho_1 H_2 - \rho_2 H_1) + (\rho_2 - \rho_1) H} (\omega_{1,i} - \omega_{2,i}) + \omega_{2,i}. \quad (4)$$

As stated by the authors, such a calibration procedure provides an approximated description of the composition of body tissues. Indeed, at conventional scanner energies (around 120 keV) the imaging process mostly involves the photoelectric effect, coherent scattering, and Compton scattering. Tissues with different compositions may thus result in similar H (this is particularly true for soft tissues). Moreover, the partial volume effect may assign an artificial H value to a voxel containing a mixture of several tissues. Schneider *et al.*¹⁴ have estimated the accuracy of their calibration method to be better than 0.04 g cm^{-3} , which corresponds to about 20–40 H units, depending on the density (slightly lower slope for denser tissues). Kanematsu *et al.*¹⁵ have estimated the precision to be 1% (about 20 H). Schaffner and Pedroni¹⁶ have estimated the accuracy to be around 1.1% for soft tissues and 1.8% for bone tissues (from 20 to 40 H).

II.B. Existing image representations in GEANT4

Once the CT image has been converted to an image of materials, different possibilities exist to insert the data into a MC simulation. In a MC simulation code, the physical world is described by means of elementary volumes of homogeneous composition. This work was elaborated using the GEANT4 toolkit⁶ but could be adapted to other simulation codes (provided that they force interactions at voxel boundaries, unlike DPM or VMC¹⁷). In GEANT4, an image of materials can be introduced using several techniques:

- (1) Box Volume (BV). This first method is straightforward. For each voxel of the image, it creates a parallelepiped box (G4Box) filled with the associated material. Memory consumption is high (about 56 bytes per voxel¹⁷) and navigation is very slow, thus preventing the use of such a representation for large images.
- (2) Parameterized Volume (PV). This method, advocated for example by Jiang and Paganetti,⁵ allows storing a single voxel representation in memory and dynamically changing its location and composition at run-time during the navigation. The main advantage of this method is high efficiency in memory space.
- (3) Isothetic Volume (IV). By merging adjacent voxels sharing similar material (with a given tolerance) into a larger voxel, it is possible to reduce the number of parallelepipeds. Hubert-Tremblay *et al.*¹⁷ have proposed the use of octree compression to merge adjacent voxels. All resulting parallelepipeds are inserted into GEANT4 by means of

the BV (or possibly PV) approach. “Isothetic” means that the image is composed of parallelepiped cells arranged with their faces parallel to the three principal axes.

- (4) Nested Parametrized Volume (NPV). While reusing the same mechanism as PV, this representation also splits the 3D volume along the three principal directions, allowing logarithmic finding of neighboring voxels.

What all of these representations have in common is that images are split into sub-volumes of homogeneous composition, which are parallelepipeds, either of the voxel size or larger. In BV, PV, and NPV all parallelepipeds have the same dimensions, while in IV parallelepipeds have different sizes (the side length can be a multiple of the initial voxel side length). The main advantage is that geometrical operations needed for particle tracking (for example, computing the intersection between a vector and a volume) are fast to compute for a parallelepiped. However, the main drawback is that all the particles are forced to stop at the boundaries of all parallelepipeds, generating a supplementary step and additional time cost, even if the two neighboring parallelepipeds share the same content. Such artificial steps occur very often as human organs are far from being parallelepipedic.

Another potential source of slowness is the navigation algorithm used to find parallelepiped neighbors when a particle moves outside a volume. GEANT4 uses a technique called SmartVoxel or voxelization, which consists of spanning the space with virtual geometrical slices. When seeking for the next volume, research is performed hierarchically, dimension by dimension. Smartless, a parameter corresponding to the average number of slices used per contained volume, defines the granularity of the voxelization. Setting a high value when using an image composed of millions of parallelepipeds leads to too many created slices, which increases memory consumption and prevents launching of the simulation. The default value in GEANT4 is 2, which is not adapted to very large geometry. As proposed in Ref. 18, a value of 0.02 was used.

III. PROPOSED APPROACH: REGIONS OF ARBITRARY SHAPE

The CT calibration accuracy estimations reported in Sec. II A before suggest that it should not be necessary to use the whole range of H and that voxels with neighboring H can be associated in a same homogeneous region. This is typically an image segmentation problem aiming at reducing the complexity of the scene while preserving overall accuracy. Our approach is based on two steps: (1) Segmenting the CT image into homogeneous regions, whatever the shape of the resulting regions (parallelepiped or not), and (2) inserting the segmented image into the simulation using a new representation that allows us to handle voxelized regions of arbitrary shape. The next section first describes the new representation proposed that allows us to handle arbitrary shaped voxelized regions in GEANT4 simulations. This method is very general

and can be used with any segmented image as input. We then describe a method used to segment a CT image into regions.

III.A. Handling segmented volumes in GEANT4 simulations

We assume here that an initial CT image has been segmented into regions of homogeneous composition, resulting in a label image in which each voxel is labeled with the index of a material. Together with this label image comes a file that associates each label with a given material composition and density. In the label image, a region is defined as a set of voxels sharing the same label, and is not necessarily a parallelepiped. Instead of providing an analytical description (such as NURBS or superquadric modeling¹⁹), we propose to describe the regions using the initial underlying discrete uniform voxel grid. We propose new geometric operators to manage such a geometry. This approach is named Segmented Volume (SV).

In GEANT4, the geometrical properties of a volume are handled by a `G4VSolid` class, which must be able to answer several geometrical queries during the navigation process. The main operations are:

- `Inside(p)`, which computes whether the point p is inside, outside, or on the surface of the volume.
- `DistanceToIn(p, v)`, which computes the distance covered by a particle at point p to enter the volume when travelling in direction v . If the line defined by (p, v) does not intersect the volume then an infinite distance is returned. Another version of `DistanceToIn` computes the shortest distance between the point p and the volume, independently of the direction. This is used as a safety distance, avoiding further computation when, for example, a shorter distance to another volume has been found previously.
- `DistanceToOut(p, v)` is similar to `DistanceToIn` and computes the distance needed by a particle at point p to move out of the volume according to the direction v . A direction-independent version is also available.

Such functions are very fast to compute if the volume is as simple as a parallelepiped (independently of its size). To represent a SV, we propose a new `G4VSolid` class, called `RegionSolid`, and we provide an efficient way to compute the previously mentioned geometric queries. Given a label image, a `RegionSolid` is created for each region in the image; it has access to the label image and to the label of the region it represents. Each `RegionSolid` then performs the computation of the different geometrical queries as follows. For `Inside(p)`, the calculation is straightforward. By rounding the coordinate of the point p according to the underlying voxel grid, one directly obtains the region to which p belongs by reading the voxel label. For `DistanceToIn` and `DistanceToOut`, we adapted a voxel-based discrete ray-tracing algorithm allowing us to compute the distance on a step-by-step basis, each step being determined according to the voxel boundaries (see Fig. 1). For the direction-independent versions, we used a distance map that stores, for

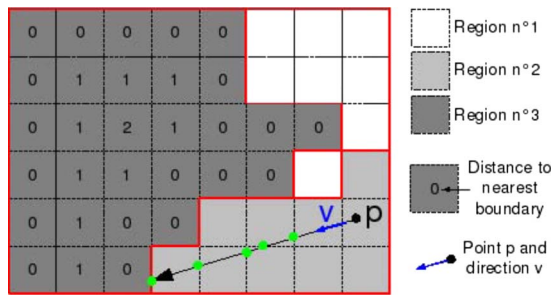


FIG. 1. Two dimensional illustration of the Segmented Volume approach. To compute the `DistanceToOut` operation from the point p and along the direction v , a discrete ray-tracing is performed (the dots on the line illustrate the geometrical steps). The numbers indicated inside the voxels in the dark region on the left represent the distance map values used for safety distance computation.

each voxel, the shortest distance to the nearest boundary of the region to which the voxel belongs (see Fig. 1). More precisely, for a voxel v belonging to region $R(v)$, the distance $d_{\min}(v)$ is the shortest distance between any location in v and any location in $\overline{R(v)}$, the complementary set of $R(v)$

$$d_{\min}(v) = \min\{d(p,q) | p \in v, q \in \overline{R(v)}\}. \quad (5)$$

Hence, for a given particle located at noninteger coordinates within a voxel, the distance is an underestimate of the real nearest distance to the boundary of the region. Such an image of distances is usually called a Distance Map and efficient algorithms to compute them have been proposed in the image processing community. We used the `INSIGHT Toolkit` (<http://www.itk.org>) implementation of Danielsson's algorithm.²⁰

Of course, the computation of these geometrical operations is longer for a `RegionSolid` than for a parallelepiped (`G4Box`). However, in the case of homogenous regions spanning multiple voxels, the technique optimizes the number of geometrical steps, which now only occur at real boundaries (between two different adjacent materials) and not at artificial boundaries (between two parallelepipeds sharing the same material).

In practice, such an approach does not involve modifying the `GEANT4` code. It is sufficient to create the new `RegionSolid` class derived from the abstract class `G4VSolid`. The distance map is computed and stored before the simulation. The two voxel matrices (the initial one composed of the matrix of labels and the distance map) are loaded and stored in memory. The `SegmentedVolume` in itself does not occupy much more space in memory than the `NPV` approach (see Sec. IV A).

III.B. Image segmentation procedure

In the image processing field, the term segmentation refers to the process of partitioning an image into multiple regions (sets of pixels) in order to decrease scene complexity by removing noise or unnecessary image details. For the sake of simplicity, we will focus only on photon beams for which the majority of physical processes depend on the elec-

tronic density of the material. Hence, the merging of two materials will be performed with a certain tolerance regarding the difference of electronic density between the voxels. For other types of beams (proton, carbon), such a step should be performed using a different density distribution, such as the stopping power density.¹⁵ Electronic density was computed with Eq. (6), where ρN_g is the number of electrons per unit volume of the mixture, Z_i is the atomic number, and A_i is the atomic weight of element i .

$$\rho_e = \rho N_g / \rho^{\text{water}} N_g^{\text{water}}, \quad N_g = N_A \sum_i \frac{\omega_i Z_i}{A_i}. \quad (6)$$

Based on such a density image, several image segmentation methods can be applied to merge homogeneous neighboring regions. Among other approaches, region-based segmentation methods are generally composed of a homogeneous criterion and a regularization one. For example, Hubert-Tremblay *et al.*¹⁷ have proposed to define a region as homogeneous if it has no density gradient value greater than a user-specified threshold [named density gradient threshold (DGT)]. Based on an octree method, the regions were constrained to be parallelepipeds. For the sake of comparison, we used this procedure for image segmentation. The resulting octree structure was used with the `IV` method and the resulting segmented image was also used with the proposed `SV` method. After segmentation, resulting images have a large number of regions (the leaves of the octree) with an averaged density. Like others authors,^{5,17} we then attributed labels according to a quantization of the range of density, leading to a discrete number of different densities and corresponding materials. Quantization was performed according to the mean density difference obtained between initial and segmented density images. Such a procedure allows us to obtain both an octree structure for the `IV` method and a label image for the `SV` one. The difference is that in our `SV` model, all parallelepipeds sharing the same label are viewed as a unique volume.

III.C. Dose scoring: Voxel and dosel grids

We decided to separate the 3D matrix of voxels describing the patient (the geometrical grid) from the 3D matrix of scoring voxels (the scoring grid). By analogy with the term "voxel" describing a volume element used to record a material description, we propose to name "dosel" any volume element used to record a deposited dose. As emphasized in Ref. 21, when high resolution is required for image description (for example when inhomogeneous materials are considered), this method allows us to gain computational time by scoring doses in dosels that are larger than voxels and thus to accelerate convergence to reduced statistical uncertainty. Note that when dealing with segmented images, we used the average density obtained after segmentation to compute the dose in order to be consistent with the way energy deposit was simulated.

Relative statistical uncertainty $\varepsilon(\mathbf{x})$ at a given dosel \mathbf{x} was estimated by Eq. (7) (see for example Ref. 22). n is the number of primary events (or history), and $d^i(\mathbf{x})$ is the de-

TABLE I. Waterbox experiment. Mean (standard deviation) relative difference between various image parametrization; differences relative to dmax are also given. Parametrizations were *single box* (SB), *box volumes* (BV), *parametrized volumes* (PV), *nested parametrized volumes* (NPV), and *segmented volumes* (SV).

Parameter	Parameter	Relative difference		Difference relative to dmax	
		mean (%)	Standard deviation	mean (%)	Standard deviation
SB	BV	1.0	0.7	0.7	0.5
SB	PV	1.0	0.8	0.7	0.5
SB	NPV	1.0	0.7	0.7	0.5
SB	SV	0.7	0.6	0.5	0.4
BV	PV	0.0	0.0	0.0	0.0
BV	NPV	0.1	0.0	0.0	0.2
BV	SV	1.0	0.8	0.7	0.5
NPV	PV	0.5	0.4	0.4	0.3
NPV	SV	1.0	0.8	0.7	0.5

posited energy in dosel \mathbf{x} at (primary) event i . Average relative uncertainty s [Eq. (8)] was computed with the method proposed by Ref. 23 for all m dosels \mathbf{x} such that $d(\mathbf{x}) > 0.5 d_{\max}$, with d_{\max} the maximum deposited dose in a dosel. More details on statistical uncertainty can be found in Ref. 24. We used mean relative difference

$$\text{MRD}(d_1, d_2) = \frac{1}{m} \sum_x \frac{|d_1(\mathbf{x}) - d_2(\mathbf{x})|}{d_1(\mathbf{x})}$$

to compare the dose distribution d_2 relatively to d_1 . For comparison purposes, we will also present the results using dose difference relatively to d_{\max} , because this form is sometimes used in the literature (Ref. 17)

$$\text{MRD}_{d_{\max}}(d_1, d_2) = \frac{1}{m} \sum_x \frac{|d_1(\mathbf{x}) - d_2(\mathbf{x})|}{d_{\max}},$$

$$\epsilon(\mathbf{x}) = \sqrt{\frac{n \sum_i d^i(\mathbf{x})^2 - (\sum_i d^i(\mathbf{x}))^2}{(n-1)(\sum_i d^i(\mathbf{x}))^2}}, \quad (7)$$

$$s = \sqrt{\frac{1}{m_{d>0.5 d_{\max}}} \sum_x (\epsilon(\mathbf{x}))^2}. \quad (8)$$

Contrary to Ref. 21, in the proposed GEANT4 implementation, adding a dosel matrix to the voxel matrix does not significantly increase the computational time (less than 10% of the total time). Each dose deposition event leads to a floating point coordinate (in the world coordinate system), which is rounded to find the correct dosel index. The memory requirement is four floating point numbers per dosel: One for the deposited energy, one for the squared energy (for computing statistical uncertainty), one temporary value, and one value storing the last hit event number as proposed in the efficient update method of Refs. 25 and 26 that we implemented in GEANT4. Finally, in GEANT4, each step is defined by a line segment determined with a pre (starting) and a post (ending) position. In order to avoid biases and as advocated in the documentation, we computed a

random location on the segment and added the current energy deposition to the dosel containing this location.

IV. EXPERIMENTS

We tested the proposed Segmented Volume in three experiments. The first experiment was the irradiation of a simple water box. The goal was to validate the approach and estimate the computational burden due to the introduction of voxels. The second experiment used a phantom. It aimed at illustrating the time decrease as a function of the number of voxels. The third experiment was performed on patient data. It illustrates the proposed method in a complex geometry with numerous heterogeneities.

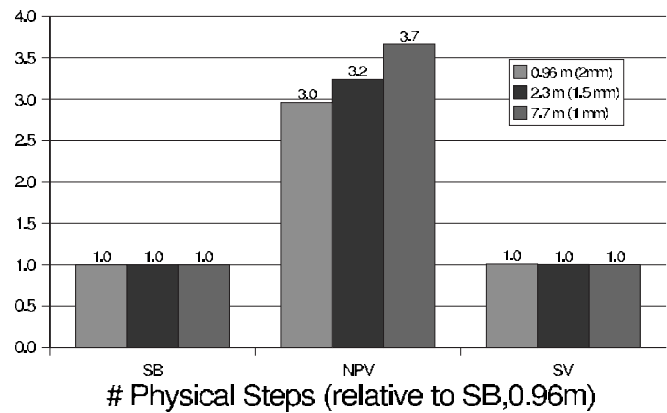
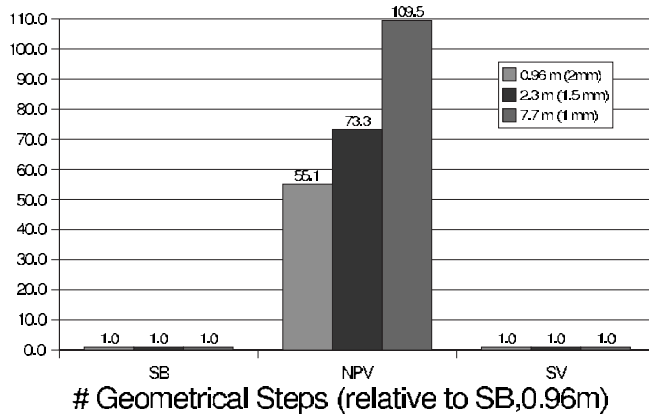
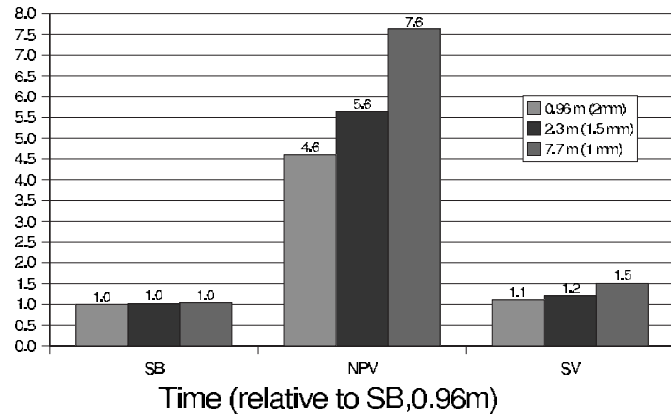
IV.A. Water box experiment

IV.A.1. Description

This first experiment aimed at illustrating the difference between nonvoxelized and voxelized geometry in terms of computation time, dose distribution, and memory consumption. It also aimed at validating the proposed method. The geometry was composed of a box of water. The beam source was a 6 MV photon conic beam with an energy spectrum obtained by MCNPX simulation of an Elekta Precise™ device. The physics list was based on the low energy electromagnetic package. The distance to axis was set to 100 cm and we used a 20 mm radius beam size (at isocenter). Sixty million primary events were simulated. The box ($160 \times 160 \times 300 \text{ mm}^3$) was described successively with a single homogeneous box (denoted by SB) or a voxelized volume with cubic voxels. Three sizes were used: 2^3 , 1.5^3 , and 1^3 mm^3 , leading to 1, 2.3, and 7.7 million voxels, respectively. Four methods were compared: Multiple G4Box (BV), parametrized volume (PV), nested parametrized volume (NPV), and segmented volume (SV). Of course, the IV model would give the same result as SB because the octree segmentation would lead to only one box. For all configurations, the deposited energy distribution was stored in a $80 \times 80 \times 150$ dosel grid with $2 \times 2 \times 2 \text{ mm}^3$ dosel size. Production cuts

TABLE II. Waterbox experiment. Time, the number of geometrical steps, and the number of physical steps (expressed relatively to the SB experiment with 0.96 million voxels), for the three different configurations (SB, NPV, and SV) and three voxel numbers (0.96, 2.3, and 7.7 million voxels).

Time	0.96 m (2mm)	2.3 m (1.5 mm)	7.7 m (1 mm)
SB	1.0	1.0	1.0
NPV	4.6	5.6	7.6
SV	1.1	1.2	1.5
Geom Steps	0.96 m (2mm)	2.3 m (1.5 mm)	7.7 m (1 mm)
SB	1.0	1.0	1.0
NPV	55.1	73.3	109.5
SV	1.0	1.0	1.0
Physic Steps	0.96 m (2mm)	2.3 m (1.5 mm)	7.7 m (1 mm)
SB	1.0	1.0	1.0
NPV	3.0	3.2	3.7
SV	1.0	1.0	1.0



were set to 0.5 mm for photons and 0.3 mm for electrons/positrons in the water box, and 2 mm for all particles outside the box. Such cuts prevent the creation of secondary particles when the energy range is below the chosen values; instead, the energy is deposited locally.

IV.A.2. Results

Table I displays the mean relative difference between the dose distribution obtained with the various parameterizations (BV, PV, NPV, SV) and without voxelization (SB). All simulations led to average relative uncertainties below 0.9%. We also computed the total dose deposited inside the whole box with the different methods and found the following relative differences: 0.2% between SB and PV (or BV), 0.18% between SB and NPV, and 0.0023% between SB and SV. Computational time, the number of geometrical and physical steps (relatively to the SB experiment with 0.96 million voxels) are given in Table II for SB, NPV, and SV configurations, and for 0.96, 2.3, and 7.7 million voxels. Memory consumption (on a 64-bit AMD Athlon PC) according to the different parametrizations is displayed in Table III.

IV.A.3. Discussion

In Table I, BV, PV, and NPV should produce exactly the same results because GEANT4 has been forced to use the same random number sequence. Indeed, the history of all particles should be identical because all are stopped at exactly the same positions, whatever the parametrization used. However, even if it came true for BV compared to PV, NPV induced a slightly different behavior. Inadequate management of some

TABLE III. Waterbox experiment. Memory (in megabytes) used for processing 1 million voxels according to the different methods. Three versions of the PV parametrization with different smartless values are indicated.

Parametrization	RAM (Mbytes)
SB (no voxels)	62
BV	1416
PV (smartless=2)	850
PV (smartless=0.2)	303
PV (smartless=0.02)	122
NPV	66
SV	70

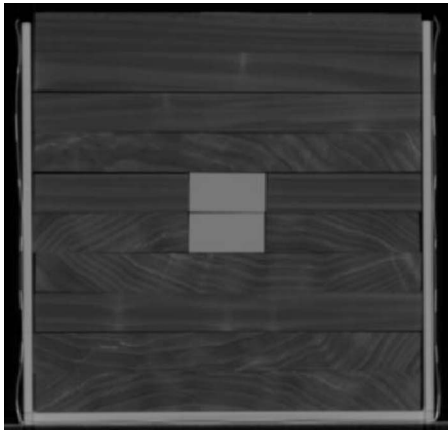


FIG. 2. Slice of the phantom used in the experiment. The phantom is composed of wood, polyethylene, and PMMA.

particular situations (a particle touching the edge of a volume but not entering it, for instance) was observed in GEANT4 when using NPV. We have proposed the use of a patch to partially correct the problem (submitted to the GEANT4 community). This patch reduces relative differences between BV/PV and NPV to less than 0.07%. We thus consider that the three parametrizations BV, PV, NPV are equivalent in terms of deposited dose.

First, we observed that dose differences between voxelized (BV, PV, NPV, SV) and nonvoxelized (SB) volumes remained equivalent or below the statistical uncertainty (1%). The number of histories (60 million) was chosen to keep statistical uncertainty below 1%. SV should also be statistically identical to SB because it removes all voxel boundaries inside the box. However, there are some approximations in the computation of safety distance based on the distance map and we observed slight differences. We recall that all the mentioned differences are made (on average) dosel by dosel. Global differences computed on the whole box were very low (<0.003% between BV and SV, for example).

Such experiments also bring to light the computational

cost of introducing voxels. For NPV, time was increased by a factor between 4 and 8 when using 0.96, 2.3, and 7.7 million voxels, respectively. We observed that the number of geometrical steps dramatically increased (by a factor of 50–100). The number of physical steps was also increased by a factor of 3 to 4. SV remained slower than SB (1.5 times slower for 7.7 million voxels) due to the burden of geometrical steps, which increases when the image is complex. The simulation is, however, about five times faster with SV than with NPV for approximately the same memory requirement as SB (Table III).

IV.B. Phantom experiment

IV.B.1. Description

In these experiments, we used a CT image of a manufactured phantom composed of wood (0.47 g cm^{-3}), polyethylene (0.9 g cm^{-3}), and PMMA (1.2 g cm^{-3}), used for portal image calibration in our radiotherapy department. The phantom image (see Fig. 2) was segmented into five materials (by adding air and graphite). The image was $512 \times 512 \times 47$ (about 12.3 million voxels) with a resolution of $0.6 \times 0.6 \times 5 \text{ mm}^3$. We compared NPV, IV, and SV methods. For IV, as only five materials were used, we used an exact octree segmentation¹⁷ with a DGT value of 0. Parameters were the same as for the previous experiment, except for the beam radius, which was 50 mm. One hundred million primary events were simulated. Dosel size was set to $2 \times 2 \times 2 \text{ mm}$. Production cuts were set to 0.01 mm for gamma, electrons, and positrons.

IV.B.2. Results

Octree compression (IV) led to about 800 000 parallelepipeds (compression ratio of about 93%, comparable to what is found in Ref. 17 for another phantom image). Simulations performed with 100 million primary particles led to average relative uncertainties below 0.8%. Table IV displays the relative dose difference, the time, and the number of geometrical and physical steps. The simulation was performed on a re-

TABLE IV. Phantom experiment. Top: Mean (standard deviation) relative difference between NPV, IV, and SV for the phantom experiment. Differences relative to dmax are also given. Bottom: Time, number of geometrical steps, and number of physical steps with NPV, IV, and SV for 1 million events.

Parameter	Parameter	Relative difference		Difference relative to dmax		
		Mean (%)	Standard deviation	Mean (%)	Standard deviation	
NPV	IV	0.92	0.67	0.68	0.53	
NPV	SV	0.93	0.72	0.68	0.53	
IV	SV	0.90	0.71	0.66	0.53	
	NPV	IV	SV	NPV/IV	NPV/SV	IV/SV
Time (mn)	216 mn	43 mn	14 mn	5.1	15.1	3.0
SG	562 million	72 million	16 million	7.8	33.9	4.4
SP	48 million	28 million	24 million	1.7	2.0	1.2

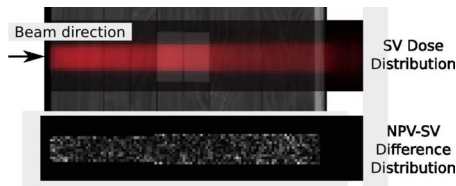


FIG. 3. Example of the dose distribution superimposed on one phantom CT slice. The corresponding dose difference distribution between NPV and SV is shown at the bottom.

mote cluster of workstations (composed of AMD Opteron, dual-core processors under Linux, 2Ghz). The time measurements were done for 1 million events. Time measurements were subject to variation due to the load of the cluster, however, the normalization of values according to the percentage of CPU used allowed us to compare simulation times.

IV.B.3. Discussion

Computational time was decreased by a factor of 15 when using SV compared to NPV. Such a performance can be explained by the large reduction in the number of steps (almost 34 times less). We note that the reduction here was superior to the one obtained in the waterbox experiment. There are more voxels (12.3 million) and the number of physical interactions is higher. Average dose relative differences between the three methods remain lower than 1% which in the order of the statistical uncertainty. Figure 3 illustrates the dose distribution in the phantom and Fig. 4 shows a depth dose distribution plot with the three methods (NPV, IV, and SV) and the corresponding differences between NPV and SV. We observed that there were no dosels with relative error greater

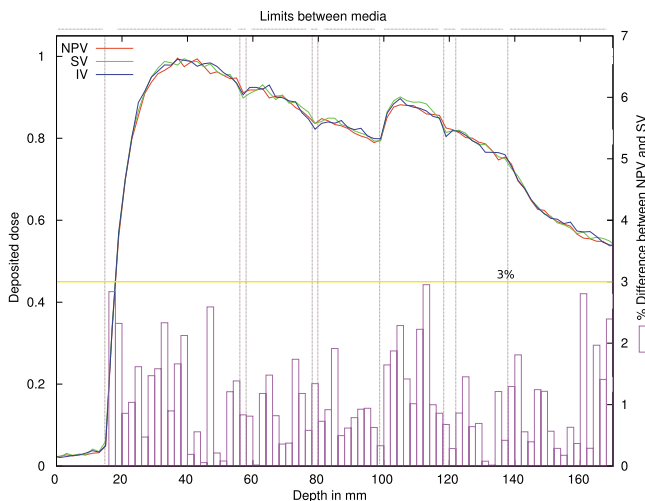


FIG. 4. Dose profile in the phantom computed with the methods NPV, SV, and IV (dose is expressed relatively to the maximum dose observed with NPV, on the left axis). Relative differences between NPV and SV are shown with vertical boxes (values are on the right axis). Vertical lines show the limits between different media.

TABLE V. Segmentation DGT (g cm^{-3}), quantization (number of materials), density differences (mean, max, standard deviation) and number of resulting boxes (octree leafs).

	DGT	Materials	Mean	Max	Standard deviation	Number of boxes
Test1	0.010	242	0.002	0.013	0.002	2,733,826
Test2	0.020	117	0.004	0.028	0.004	2,069,821
Test3	0.025	79	0.005	0.041	0.006	1,855,670
Test4	0.050	41	0.010	0.079	0.012	1,233,620
Test5	0.075	27	0.014	0.120	0.017	934,133
Test6	0.100	16	0.027	0.181	0.030	750,708

than 3%. The effect of the boundaries between different media can be observed with the vertical lines.

IV.C. CT image experiment

IV.C.1. Description

For the third series of simulations, we used a thorax CT image of a patient with nonsmall cell lung cancer. Initial image size was $512 \times 512 \times 77$ (more than 20 million voxels) with a resolution of $1.2 \times 1.2 \times 5 \text{ mm}^3$. We reduced the number of voxels by segmenting the air region surrounding the

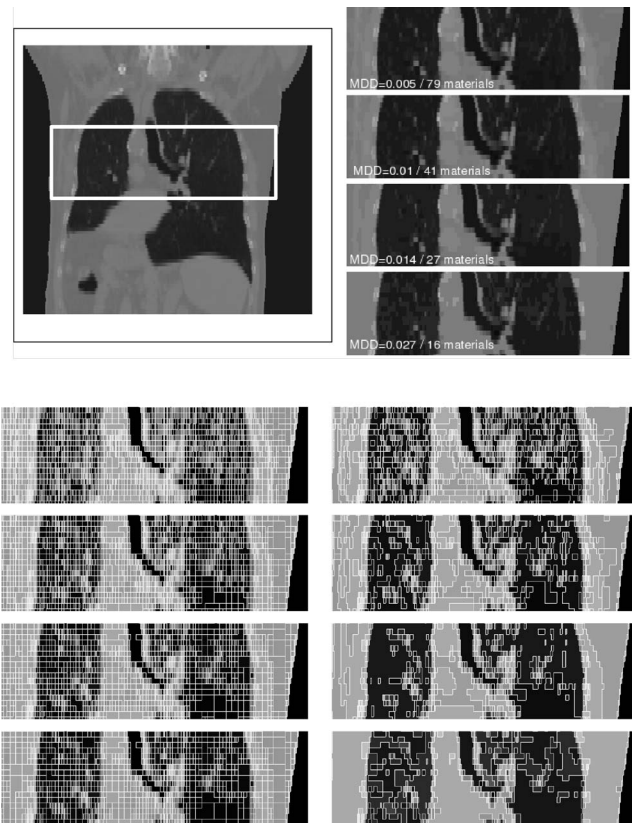


FIG. 5. Top left: Original CT slice. Top right: The four images show the segmentation results obtained with different DGT values. The mean density difference and corresponding number of materials are indicated on the images (see Table V). Bottom left: Parallelepiped leaves resulting from the octree procedure. Bottom right: The same images after quantization procedure. Simplification is especially visible on the last images.

TABLE VI. CT experiment. Dose relative difference between NPV, IV and SV, according to different segmentations. Left: Differences between methods using the same segmentation. Right: Differences relative to the reference NPV with the test 1 case.

	Parameter	Parameter	Relative difference		Difference relative to dmax	
			mean (%)	Standard deviation (%)	mean (%)	Standard deviation (%)
Test 1	NPV	IV	1.0	0.8	0.7	0.6
242 materials	NPV	SV	1.1	0.9	0.8	0.6
	IV	SV	1.1	0.8	0.8	0.6
Test 2	NPV	IV	1.1	0.8	0.7	0.6
117 materials	NPV	SV	1.1	0.9	0.8	0.6
	IV	SV	1.1	0.8	0.8	0.6
Test 3	NPV	IV	1.0	0.8	0.7	0.6
79 materials	NPV	SV	1.1	0.9	0.8	0.6
	IV	SV	1.1	0.9	0.8	0.6
Test 4	NPV	IV	1.0	0.8	0.7	0.6
41 materials	NPV	SV	1.2	0.9	0.8	0.6
	IV	SV	1.1	0.9	0.8	0.6
Test 5	NPV	IV	1.1	0.8	0.7	0.6
27 materials	NPV	SV	1.2	0.9	0.8	0.6
	IV	SV	1.2	0.9	0.8	0.6
Test 6	NPV	IV	1.1	0.8	0.7	0.6
16 materials	NPV	SV	1.2	0.9	0.8	0.6
	IV	SV	1.2	0.9	0.8	0.6
SV (ref=test1/NPV)						
			Relative difference		Difference relative to dmax	
			mean (%)	Standard deviation (%)	mean (%)	Standard deviation (%)
Test 1			1.1	0.9	0.8	0.6
Test 2			1.1	0.9	0.8	0.6
Test 3			1.2	0.9	0.8	0.6
Test 4			1.3	1.1	0.9	0.7
Test 5			1.5	1.4	1.0	0.9
Test 6			1.5	1.4	1.0	0.9
IV (ref=test1/NPV)						
			Relative difference		Difference relative to dmax	
			mean (%)	Standard deviation (%)	mean (%)	Standard deviation (%)
Test 1			1.0	0.8	0.7	0.6
Test 2			1.1	0.8	0.7	0.6
Test 3			1.1	0.9	0.8	0.6
Test 4			1.2	1.1	0.8	0.7
Test 5			1.4	1.4	1.0	0.9
Test 6			1.4	1.3	1.0	0.8

patient (according to the method described in Ref. 27) and kept the bounding box corresponding to $349 \times 228 \times 77$ voxels (about 6 million). After CT calibration,¹⁴ six segmentations were performed with the octree method according to six DGT parameters (see Table V and Fig. 5). In this figure, we do not show all segmentations because they are hardly visually distinguishable from the original image. Three methods were compared for dose and timing: NPV, IV, and SV. One hundred million primary events were simulated. Dose

size was set to $2.5 \times 2.5 \times 5 \text{ mm}^3$ (about 1.3 million dosels). Other parameters were the same as for the previous experiment.

IV.C.2. Results

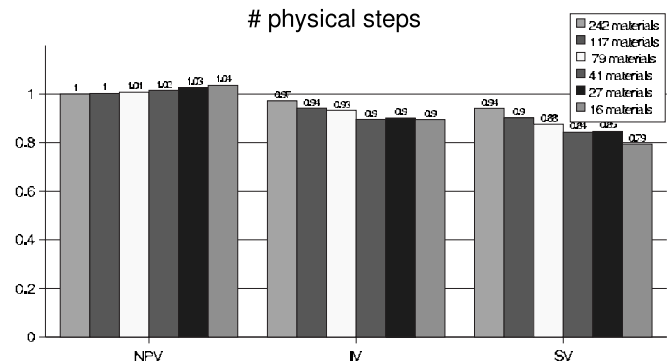
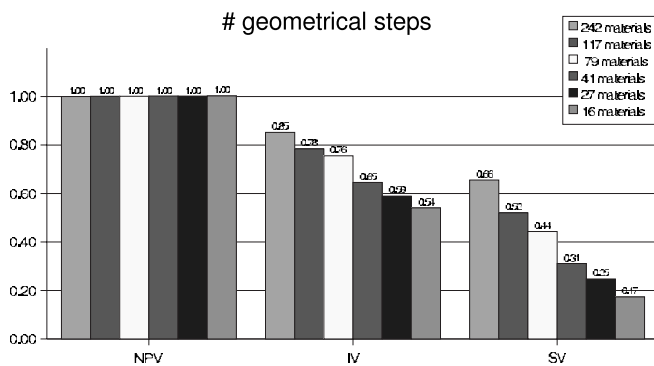
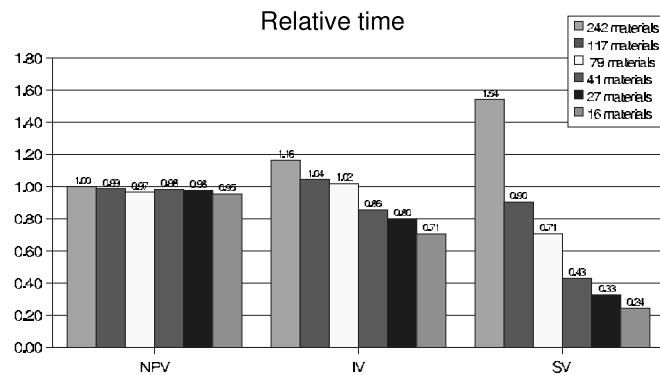
All 18 simulations (three methods, six cases) led to average relative uncertainties below 0.9%. Table VI displays the dose relative differences and Table VII the computational

TABLE VII. Time, number of geometrical steps and number of physical steps (expressed relatively to the NPV case with 242 materials), for the three different configurations (NPV, IV, SV) and the six segmentation cases.

Time	242 mat.	117 mat.	79 mat.	41 mat.	27 mat.	16 mat.
NPV	1.0	1.0	1.0	1.0	1.0	1.0
IV	0.9	1.0	1.0	1.2	1.3	1.4
SV	0.6	1.1	1.4	2.3	3.1	4.1

Geom S	242 mat.	117 mat.	79 mat.	41 mat.	27 mat.	16 mat.
NPV	1	1	1	1	1	1
IV	0.85	0.78	0.76	0.65	0.59	0.54
SV	0.66	0.52	0.44	0.31	0.25	0.17

Phys S	242 mat.	117 mat.	79 mat.	41 mat.	27 mat.	16 mat.
NPV	1	1	1.01	1.02	1.03	1.04
IV	0.97	0.94	0.93	0.9	0.9	0.9
SV	0.94	0.9	0.88	0.84	0.85	0.79



time according to the different segmentations for NPV, IV, and SV methods. Time is expressed relatively to NPV and test 1 experiment.

IV.C.3. Discussion

The mean accuracy in mass density during the segmentation stage ranged from 0.002 to 0.027 g cm⁻³. The octree stage yielded between 750 000 and nearly 2 000 000 boxes. Table VII illustrates that using SV with a reduced number of materials allowed us to reduce the computational time by up to a factor greater than 4. Using the octree structure also decreased the time by up to a factor of approximately 1.5. The gain is attributable to the large decrease in the number of geometrical steps; the number of physical steps only slightly decreases. We also observed that for excessive numbers of materials, the methods are not efficient and can even lead to increased computing time (test 1). We observed that the dose distribution differences between NPV, IV, and SV methods remained below 1.2% (left part of Table VI). In this case, this is the same material approximation and, as in the phantom experiment, differences are in the order of the uncertainty (which is below 0.9%). In the right part of Table VI, dose differences due to material approximation can be observed and range from 1.1% to 1.5%. Figure 6 illustrates the experiment with profiles: In the upper part, electronic density profiles are displayed for reference image, test no 5 and test no 6. The approximation due to the segmentation part can be observed (note that the segmentation was performed in 3D,

which explain that in the right part of the figure, the segmentation n°6 seems crude). In the bottom part of the figure, deposited dose distribution profiles are shown for test no 1 compared to test no 5 and 6, with the corresponding differences between NPV and RV. In this example, some differences are greater than 3% with test no 6, while this is not the case with test no 5. We computed that 90% of the dosels in test no 6 have a relative dose difference lower than 3%. Maximum differences were greater than 7% for about 50 dosels and can reach 10% in four dosels. It is, however, difficult to separate what is due to statistical uncertainties (around 0.9%) from what is due to NPV versus SV implementation (maybe about 0.5%) and what is due to material approximation. Note that Ref. 17 also observed that the mean dose difference expressed in percent of the maximum is around 1%, which is in the same order as our observation. More validation are still needed to compare the different approaches according to experimentally measured data in such very inhomogeneous media.

Finally, the gain of computational time with the proposed method increases almost linearly according to the parameter DGT. This parameter is linked to the number of regions of the segmentation. For high DGT values, a small number of regions is obtained and the proposed method is faster. However, dose differences increase as the image is simplified. The image segmentation parameters (DGT here) can thus be used to control the tradeoff between speed and desired accuracy.

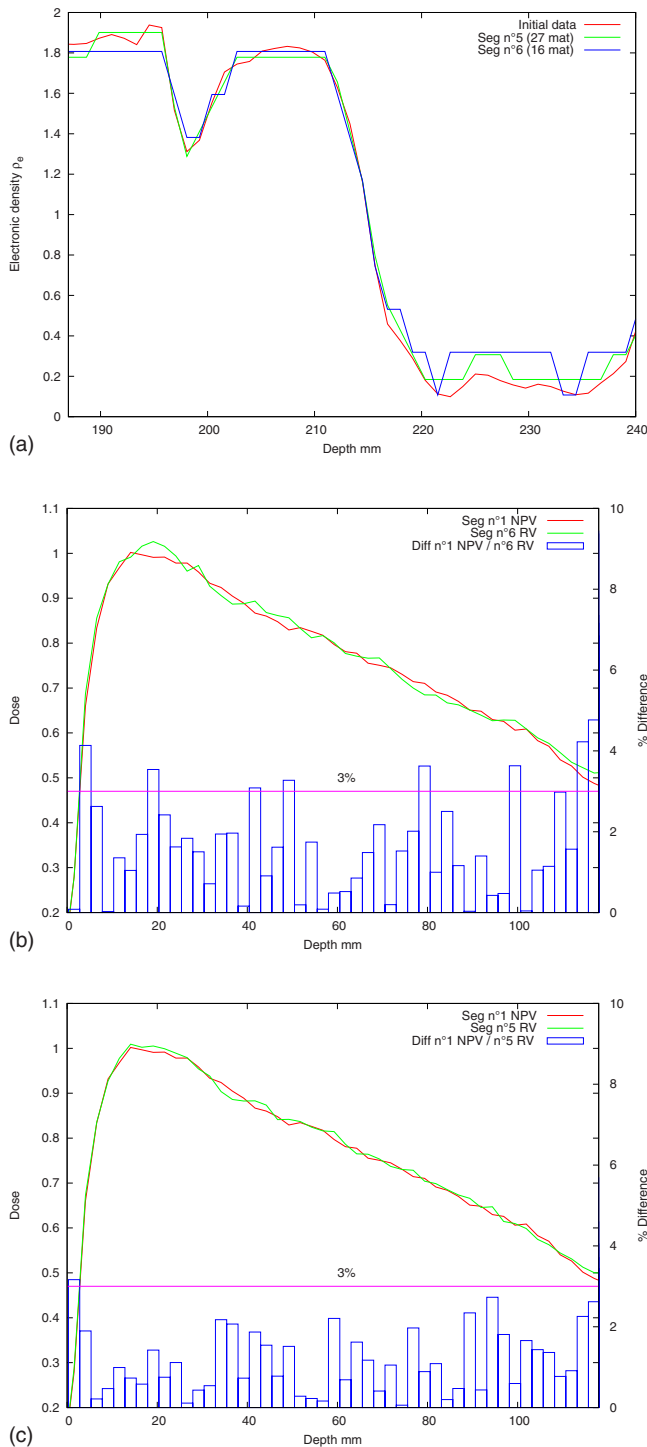


FIG. 6. (Top) Electronic density profiles for initial image data and tests n°5 and 6. (Bottom) Deposited dose profiles for test n°1 with NPV and tests n°5 and n°6 with RV. Corresponding differences are shown with boxes.

V. CONCLUSION

We have proposed a method to decrease the computational time required for GEANT4 simulations involving a 3D image-based description of the scene, such as a CT image of a phantom or a patient. Our method consists in representing the matrix of voxels with regions having specific boundary-

finding functions based on discrete ray-tracing. It is different from previously published methods because the transportation algorithm is not modified. We have also described experiments permitting us to validate the proposed method in different configurations. According to the image segmentation procedure, the proposed method allowed us to eliminate the MC steps required at artificial interfaces (between two voxels sharing the same material) until reaching an optimal number of geometrical steps. We are able to decrease the computational time by up to a factor of 15 (in the phantom case involving few materials).

The gain still remains a tradeoff between time and accuracy, with the reduction in the number of different materials leading to larger speed up. We want to emphasize that the main goal of this article was not the in depth study of the influence of this segmentation stage on final simulation results. The loss of accuracy due to the material simplification still needs to be evaluated for each application: It is the responsibility of the user to decide if dose differences that occur between NPV and SV are acceptable or not for a given application. For example, scene simplification will probably not have the same importance for dosimetric or for imaging applications. As in the method DOSSCORE proposed by Smedt *et al.*,¹² the speed gain is much more significant for weakly inhomogeneous medias (factor of 15). However, it also remains interesting (reduction in time of 3 to 4) for patient data.

On patient data, the segmentation of the CT image could be difficult to perform automatically *a priori* because of the noise. Manual segmentation can also be employed. Other criteria than the DGT of homogeneous criteria could be used (such as region density variance). Generally, segmentation combines a homogeneity criterion (internal energy) with a shape regularization (external energy) allowing us to introduce a certain *a priori* in the region shape. Finding the best way to segment an image could be the subject of another study.

The proposed approach has been applied to the GEANT4 code but should also be applicable to other simulation codes. It does not require us to modify the transportation algorithm. It is not dedicated to accelerating radiotherapy simulations only and is also applicable to other simulations, for example PET imaging with the GATE software.¹⁸ Finally, even with the proposed technique, complete simulation still remains relatively slow. Other acceleration techniques (variance reduction, tracking cuts) must be used to further speed up the whole process. The particle navigation algorithm⁵ should still be optimized with the proposed SV approach. It would accelerate the time reduction. A discrete ray-tracing algorithm faster than the simple one we used should also contribute to further decrease computational time. The method proposed here is available within an open source licence on the following website: <http://www.creatis.insa-lyon.fr/rio/THIS>. The proposed method has been proposed to the OpenGate collaboration for further study and will be introduced in a future release of the GATE¹⁸ platform.

- ^{a)} Author to whom all correspondence should be addressed. Electronic mail: david.sarrut@creatis.insa-lyon.fr
- ¹ F. Verhaegen and S. Devic, "Sensitivity study for CT image use in Monte Carlo treatment planning," *Phys. Med. Biol.* **50**, 937–946 (2005). Special Issue: International Workshop on current topics in Monte Carlo treatment planning.
- ² H. Paganetti, H. Jiang, J. A. Adams, G. T. Chen, and E. Rietzel, "Monte Carlo simulations with time-dependent geometries to investigate effects of organ motion with high temporal resolution," *Int. J. Radiat. Oncol., Biol., Phys.* **60**, 942–950 (2004).
- ³ I. Pshenichnov, I. Mishustin, and W. Greiner, "Neutrons from fragmentation of light nuclei in tissue-like media: A simulation with the geant4 toolkit," *Phys. Med. Biol.* **50**(23), 5493–5507 (2005).
- ⁴ S. Agostinelli *et al.*, "Geant4 - a simulation toolkit," *Nucl. Instrum. Methods A* **506**(3), 250–303 (2003).
- ⁵ H. Jiang and H. Paganetti, "Adaptation of GEANT4 to Monte Carlo dose calculations based on CT data," *Med. Phys.* **31**, 2811–2818 (2004).
- ⁶ J. Allison, K. Amako, J. Apostolakis, H. Araujo, P. Arce Dubois, M. Asai, G. Barrand, R. Capra, S. Chauvie, R. Chytrcek, G. A. P. Cirrone, G. Cooperman, G. Cosmo, G. Cuttone, G. G. Daquino, M. Donszelmann, M. Dressel, G. Folger, F. Foppiano, J. Generowicz, V. Grichine, S. Guatelli, P. Gupte, A. Heikkinen, I. Hrivnacova, A. Howard, S. Incerti, V. Ivanchenko, T. Johnson, F. Jones, T. Koi, R. Kokoulin, M. Kossov, H. Kurashige, V. Lara, S. Larsson, F. Lei, O. Link, F. Longo, M. Maire, A. Mantero, B. Mascialino, I. McLaren, P. Mendez Lorenzo, K. Minamimoto, K. Murakami, P. Nieminen, L. Pandola, S. Parlati, L. Peralta, J. Perl, A. Pfeiffer, M. G. Pia, A. Ribon, P. Rodrigues, G. Russo, S. Sadilov, G. Santin, T. Sasaki, D. Smith, N. Starkov, S. Tanaka, E. Tcherniaev, B. Tome, A. Trindade, P. Truscott, L. Urban, M. Verderi, A. Walkden, J. P. Wellisch, D. C. Williams, D. Wright, and H. Yoshida, "Geant4 developments and applications," *IEEE Trans. Nucl. Sci.* **53**, 270–278 (2006).
- ⁷ E. Poon, J. Seuntjens, and F. Verhaegen, "Consistency test of the electron transport algorithm in the GEANT4 Monte Carlo code," *Phys. Med. Biol.* **50**, 681–694 (2005).
- ⁸ E. Poon and F. Verhaegen, "Accuracy of the photon and electron physics in Geant4 for radiotherapy applications," *Med. Phys.* **32**, 1696–1711 (2005).
- ⁹ M. Ljungberg, S. E. Strand, and M. A. King, *Monte-Carlo Calculation in Nuclear Medicine*, Medical science series (Institute of Physics Publishing, Bristol and Philadelphia, 1998).
- ¹⁰ N. Freud, J. M. Létang, and D. Babot, "A hybrid approach to simulate x-ray imaging techniques, combining Monte Carlo and deterministic algorithms," *IEEE Trans. Nucl. Sci.* **52**, 1329–1334 (2005).
- ¹¹ L. Wang, C. S. Chui, and M. Lovelock, "A patient-specific Monte Carlo dose-calculation method for photon beams," *Med. Phys.* **25**, 867–878 (1998).
- ¹² B. De Smedt, N. Reynaert, W. De Neve, and H. Thierens, "DOSSCORE: An accelerated DOSXYZnrc code with an efficient stepping algorithm and scoring grid," *Phys. Med. Biol.* **49**, 4623–4635 (2004).
- ¹³ U. Schneider, E. Pedroni, and A. Lomax, "The calibration of CT Hounsfield units for radiotherapy treatment planning," *Phys. Med. Biol.* **41**, 111–124 (1996).
- ¹⁴ W. Schneider, T. Bortfeld, and W. Schlegel, "Correlation between CT numbers and tissue parameters needed for Monte Carlo simulations of clinical dose distributions," *Phys. Med. Biol.* **45**, 459–478 (2000).
- ¹⁵ N. Kanematsu, N. Matsufuji, R. Kohno, S. Minohara, and T. Kanai, "A CT calibration method based on the polybinary tissue model for radiotherapy treatment planning," *Phys. Med. Biol.* **48**, 1053–1064 (2003).
- ¹⁶ B. Schaffner and E. Pedroni, "The precision of proton range calculations in proton radiotherapy treatment planning: Experimental verification of the relation between ct-hu and proton stopping power," *Phys. Med. Biol.* **43**, 1579–1592 (1998).
- ¹⁷ V. Hubert-Tremblay, L. Archambault, D. Tubic, R. Roy, and L. Beaulieu, "Octree indexing of dicom images for voxel number reduction and improvement of Monte Carlo simulation computing efficiency," *Med. Phys.* **33**, 2819–2831 (2006).
- ¹⁸ S. Jan, G. Santin, D. Strul, S. Staelens, K. Assié, D. Autret, S. Avner, R. Barbier, M. Bardès, P. M. Bloomfield, D. Brasse, V. Breton, P. Bruyn-donckx, I. Buvat, A. F. Chatzioannou, Y. Choi, Y. H. Chung, C. Comtat, D. Donnarieix, L. Ferrer, S. J. Glick, C. J. Groiselle, D. Guez, P. F. Honore, S. Kerhoas-Cavata, A. S. Kirov, V. Kohli, M. Koole, M. Krieger, D. J. van der Laan, F. Lamare, G. Largeron, C. Lartizien, D. Lazaro, M. C. Maas, L. Maigne, F. Mayet, F. Melot, C. Merheb, E. Pennacchio, J. Perez, U. Pietrzyk, F. R. Rannou, M. Rey, D. R. Schaart, C. R. Schmidlein, L. Simon, T. Y. Song, J. M. Vieira, D. Visvikis, R. Van de Walle, E. Wieës, and C. Morel, "GATE: A simulation toolkit for PET and SPECT," *Phys. Med. Biol.* **49**, 4543–4561 (2004).
- ¹⁹ J. Peter, M. P. Tornai, and R. J. Jaszczak, "Analytical versus voxelized phantom representation for Monte Carlo simulation in radiological imaging," *IEEE Trans. Med. Imaging* **19**, 556–564 (2000).
- ²⁰ P. E. Danielsson, "Euclidean distance mapping," *Comput. Graph. Image Process.* **14**, 227–248 (1980).
- ²¹ B. De Smedt, B. Vanderstraeten, N. Reynaert, W. De Neve, and H. Thierens, "Investigation of geometrical and scoring grid resolution for Monte Carlo dose calculations for IMRT," *Phys. Med. Biol.* **50**, 4005–4019 (2005).
- ²² C. M. Ma, J. S. Li, T. Pawlicki, S. B. Jiang, J. Deng, M. C. Lee, T. Koumrian, M. Luxton, and S. Brain, "A Monte Carlo dose calculation tool for radiotherapy treatment planning," *Phys. Med. Biol.* **47**, 1671–1689 (2002).
- ²³ D. W. O. Rogers and R. Mohan, "Questions for comparison of clinical Monte Carlo codes," W. Schlegel and T. Bortfeld, editors, *13th Int. Conf. on the Use of Computer in Radiation Therapy (ICCR)*, Springer, pp. 120–122, Heidelberg, 2000.
- ²⁴ I. J. Chetty, M. Rosu, M. L. Kessler, B. A. Fraass, R. K. Ten Haken, F. M. Spring Kong, and D. L. McShan, "Reporting and analyzing statistical uncertainties in Monte Carlo-based treatment planning," *Int. J. Radiat. Oncol., Biol., Phys.* **65**, 1249–1259 (2006).
- ²⁵ B. R. B. Walters, I. Kawrakow, and D. W. O. Rogers, "History by history statistical estimators in the beam code system," *Med. Phys.* **29**, 2745–2752 (2002).
- ²⁶ J. Sempau, A. Sánchez-Reyes, F. Salvat, H. O. ben Tahar, S. B. Jiang, and J. M. Fernández-Varea, "Monte Carlo simulation of electron beams from an accelerator head using penelope," *Phys. Med. Biol.* **46**, 1163–1186 (2001).
- ²⁷ D. Sarrut, V. Boldea, S. Miguet, and C. Ginestet, "Simulation of 4D CT images from deformable registration between inhale and exhale breath-hold CT scans," *Med. Phys.* **33**, 605–617 (2006).